Innov Biosyst Bioeng, 2019, vol. 3, no. 3, 152–167
doi: 10.20535/ibb.2019.3.3.177976
UDC 532.5, 577.3

Original article

MAXIMAL SPEED OF UNDERWATER LOCOMOTION

I. Nesteruk*

Institute of Hydromechanics, National Academy of Sciences of Ukraine, Kyiv, Ukraine
Igor Sikorsky Kyiv Polytechnic Institute, Kyiv, Ukraine

*Corresponding author: inesteruk@yahoo.com

Received 9 September 2019; Accepted 24 September 2019

Background. An increasing interest in unmanned underwater vehicles continues to draw attention to swimming in aquatic animals. Their high speed continues to surprise researchers. In particular, the high dolphin speed caused a series of attempts to explain its paradox, which continues to this day. Some researchers believe that even rigid bodies, shaped like water animals, provide an attached flow pattern, as opposed to the widespread view of the inevitable separation. The possible explanation may be in the perfect body form, which provides an attached flow pattern (without boundary layer separation). Elongated unseparated shapes can not only reduce the pressure drag but also delay the laminar-to-turbulent transition in the boundary layer, significantly reducing the friction drag. Thus, the highest possible swimming speeds are expected in aquatic animals.
Objective. We will try to prove that the low drag and the high speed of aquatic animals can only be ensured by their unseparated shape (as a rigid body), neglecting flexibility and compliance.
Methods. We will use: a) shape calculations of special bodies of revolution with negative pressure gradients near the tail similar to fish trunks with the use of the developed before approach; b) the known drag estimations of such shapes for laminar and turbulent cases; c) the swimming power balance and the theory of ideal propeller; d) statistical analysis of available data about the length, the speed and the aspect ratio of aquatic animals.
Results. The swimming speed of most aquatic animals is proportional to the length of the body in power 7/9. The exception is whale locomotion that occurs in turbulent mode at supercritical Reynolds numbers.
Conclusions. The perfect body shapes of most aquatic animals provide an attached laminar flow pattern. Estimated maximum speeds for laminar and turbulent cases show that the special shaped unseparated hulls can greatly increase the speed of underwater vehicles and SWATH ships. Further increase in speed can be achieved by using supercavitation and greater than animal capacity-efficiency.

Keywords: water animal locomotion; drag reduction; unseparated shapes; cavitation; high-speed underwater vehicles.

Introduction

An increasing interest in unmanned underwater vehicles continues to draw attention to swimming in aquatic animals. At one time, the high speed of the dolphin surprised Gray [1] and caused a series of attempts to explain his paradox, which continues to this day [2–6]. In particular, some researchers believe that even rigid bodies, shaped like water animals, provide an attached flow pattern [7–12], as opposed to the widespread view of the inevitable separation [13]. Elongated unseparated shapes can not only reduce the pressure drag but also delay the laminar-to-turbulent transition in the boundary layer, significantly reducing the friction drag [10, 11, 14]. Thus, the highest possible swimming speeds are expected in aquatic animals. In order to investigate their dependence on the body length, a kind of theoretical and statistical analysis was carried out. Maximal speeds for the attached laminar and turbulent hulls were estimated and compared with supercavitating ones.

Materials and Methods

Calculations of the special shaped bodies of revolution

Special shaped rigid bodies of revolution similar to some fish shapes were calculated with the use of distributions of the sources and sinks on the axis of symmetry. The stream function of the axisymmetric potential flow of the inviscid incompressible fluid was represented as follows [15, 9]:

$$\Psi(x,r) = 0.5r^2 + \beta_1 u(x_*) - 0.75E\{a[F_1(x_*) - F_1(0)] + a_1[F_1(1) - F_1(x_*)] + 2(ax + 2c)[F_2(x_*) - F_2(0)] + 2a_1(x-1)[F_2(1) - F_2(x_*)]\},$$

$$\beta_1 = 0.75E[ax_*^2 + 4cx_* - a_1(x_* - 1)^2],$$

$$u(s) = \sqrt{r^2 + (s-x)^2},$$

$$F_1(s) = 2u^3(s)/3,$$

$$F_2(s) = 0.5(s-x)u(s) + 0.5r^2 \ln[s - x + u(s)].$$

Here x, r are cylindrical coordinates. The corresponding axisymmetric body radius $R(x)$, flow velocity components v_x, v_r and pressure coefficient on the surface were calculated with the use of following equations:

$$\Psi(x, R(x)) = 0, \quad v_x = \frac{1}{r}\frac{\partial \Psi}{\partial r}, \quad v_r = -\frac{1}{r}\frac{\partial \Psi}{\partial x},$$

$$C_p(x) = \frac{2[P(x) - P_\infty]}{\rho U^2} = 1 - {v_x}^2(x, R(x)) - {v_r}^2(x, R(x)).$$

Here P and P_∞ are pressures on the body surface and in the ambient flow respectively, U is the speed of steady motion, ρ is the density of water. Varying the values of constant parameters x_*, a, a_1, c different closed $(R(L) = 0)$ and unclosed $(R(L) > 0)$ shapes can be obtained (L is the body length). The links between these parameters are discussed in [9], but every new shape calculation needs some numerical experiments.

Calculation results for different values of the aspect ratio $\lambda = L/D$ (D is the maximal body diameter) are shown in Fig. 1. Some other examples can be found in [9, 10, 12]). The pressure distributions on these bodies have a negative pressure gradient near the tail (see dashed lines representing the pressure coefficient C_P).

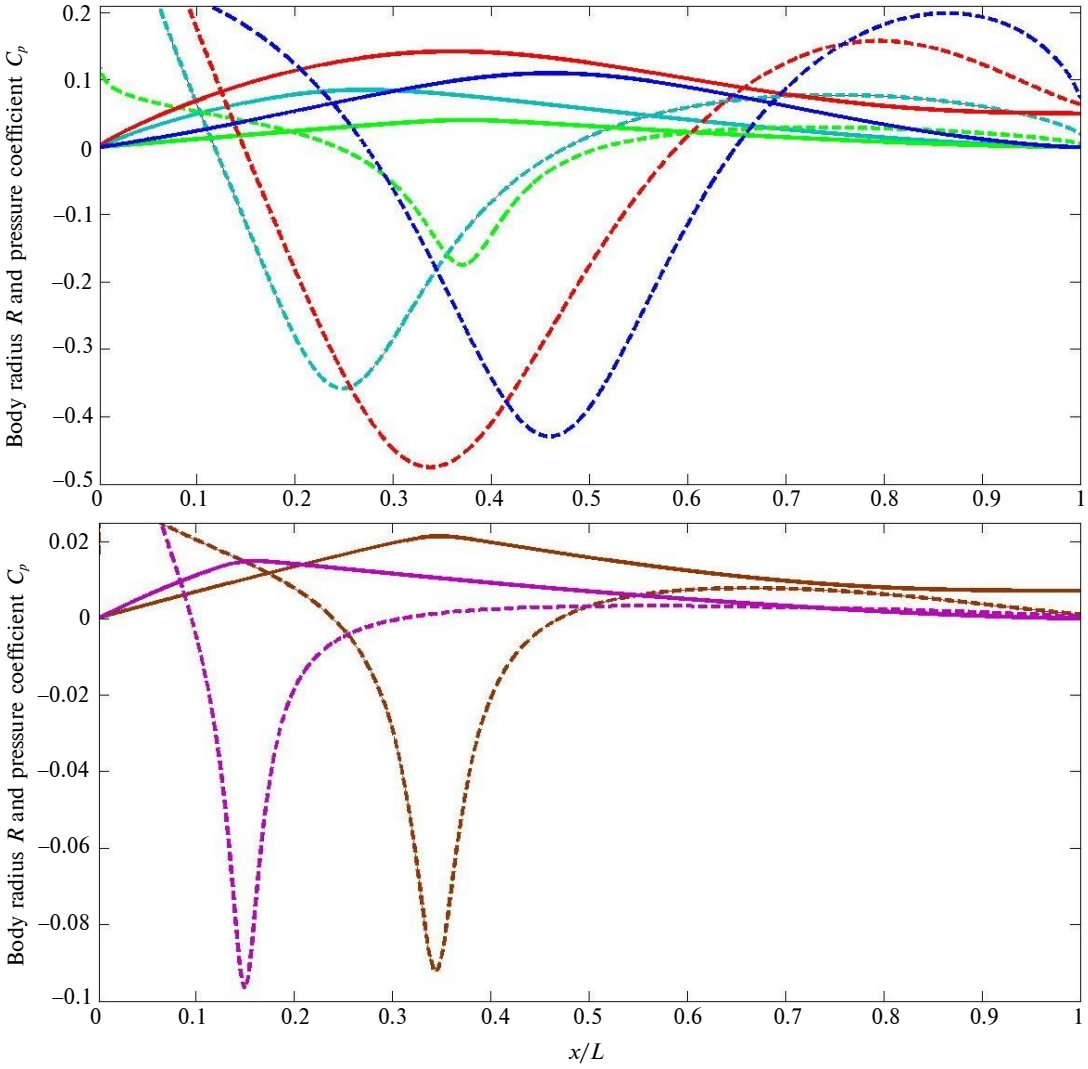

Figure 1: Special shaped bodies of revolution. Radius R (solid lines) and pressure coefficient C_P (dashed lines) versus dimensionless axis coordinate x/L

Unseparated unclosed body UA-2 ($L/D = 3.52$; red lines). Closed bodies: UA-4.5c "Albacore" ($L/D = 4.5$; dark blue lines); UA-5.9c "Blue shark" ($L/D = 5.9$; blue lines); UA-12.4c "Sailfish" ($L/D = 12.4$; green lines); UA-33.3c "Largehead hairtail" ($L/D = 33.3$; magenta lines). Unclosed body UA-23.3 ($L/D = 23.3$; brown lines)

Shapes with similar pressure distributions near the trailing have been calculated [16] and tested in wind tunnels [9, 12, 17, 18]. In particular, Goldschmied body [17] revealed the attached flow patterns only with the use of boundary layer suction. In comparison, the tests of UA-2 body showed unseparated flows without any boundary layer control methods [9, 12]. Thus, we expect that similar slender bodies (e.g., shown in Fig. 1) can also ensure attached flows due to their special rigid shape only. In this paper, we do not consider the drag reduction connected with flexible shapes (as, e.g., in [1]) or animal body compliance (as, e.g., in [19]). In order to use the theoretical drag estimations, presented in the next Section, we will also limit our study to only sufficiently slender bodies ($L/D \geq 4$ or $D/L \leq 0.25$).

Drag estimations on slender unseparated bodies of revolution

To estimate laminar frictional drag on a slender unseparated body of revolution, we can use the Mangler–Stepanov transformations [20], which reduce the rotationally symmetric boundary-layer equations to a two-dimensional case. Coordinate x for the rotationally symmetric boundary-layer (calculated along the body contour) and the corresponding two-dimensional coordinate $\bar{x}$, flow velocity at the outer edge of the boundary layer, the displacement thickness and the skin-friction coefficient are related as follows [20]:

$$\bar{x} = \int_0^x R^2(\xi)d\xi, \quad \bar{U}_{\text{out}} = U_{\text{out}}, \qquad \delta^* = \frac{\bar{\delta}^*}{R(x)}, \quad \tau_w = \bar{\tau}_w R(x). \tag{1}$$

All the values in (1) are dimensionless, based on the body length L, the ambient flow velocity U_∞ and $0.5\rho U_\infty^2$; dashed values correspond to 2D boundary layer. These equations are valid for an arbitrary rotationally symmetric body provided that the thickness of the boundary layer is small in comparison with the radius, i.e. the flow has to be unseparated. For a slender body, the coordinate x can be calculated along the body's axis and the velocity U_{out} can be supposed to be equal to unity, neglecting the thickness of the boundary layer and the pressure distribution peculiarities [21]. From the second equation (1) the value of $\bar{U}_{\text{out}}$ will also be equal to unity, i.e., the rotationally symmetric boundary layer on a slender body can be reduced to the flat-plate one [10, 14, 22]. According to the Blasius solution $\bar{\tau}_w = 0.664(\bar{x})^{-1/2}\,\text{Re}_L^{-1/2}$ for a laminar flow, where the Reynolds number $\text{Re}_L = U_\infty L/\nu$ and ν is the kinematic viscosity [20]. Introducing the variable x and using (1) yields the following formula for the laminar skin-friction drag coefficients of a slender rotationally symmetric body [10, 14]:

$$C_L = \frac{2X}{\rho U_\infty^2 L^2} = 2\pi\int_0^1 R(x)\tau_w(x)dx = \frac{4.172}{\sqrt{\text{Re}_L}}\int_0^1 R^2(x)\left[\int_0^x R^2(\xi)d\xi\right]^{-1/2} dx = 8.344\sqrt{\frac{V}{\pi L^3\,\text{Re}_L}}. \tag{2}$$

With the use of dimensionless values based on the body volume V, (2) can be rewritten as follows [10, 11, 14]:

$$C_V = \frac{4.7}{\sqrt{\text{Re}_V}}, \quad \text{Re}_V = \frac{UV^{1/3}}{\nu}. \tag{3}$$

Note that the volumetric frictional drag coefficient C_V does not depend on the slender body shape provided its volume remains constant. This is valid for laminar attached boundary layer and at limited Re_V, only.

Eq. (3) was compared with the Hoerner formula [23] for the total laminar drag X on standard bodies of revolution (e.g. ellipsoids):

$$C_S = \frac{2X}{\rho U^2 S} = C_{fl}[1 + 1.5(D/L)^{1.5}] + 0.11(D/L)^2, \qquad C_{fl} = \frac{1.328}{\sqrt{\text{Re}_L}}. \tag{4}$$

(S is the body surface area). Good agreement occurs for slender shapes when the term $0.11(D/L)^2$ (connected with separation) can be neglected (see upper dashed lines in Fig. 2).

For a turbulent boundary layer, Hoerner proposed another empirical formula [23]:

$$C_S = C_{ft}[1+1.5(D/L)^{1.5} + 7(D/L)^3], \; C_{ft} = \frac{0.0307}{\text{Re}_L^{1/7}}. \tag{5}$$

Eqs. (4) and (5) were used to estimate the drag on standard bodies of revolution with the values D/L coinciding with ones for the closed special shaped bodies of revolution shown in Fig. 1. Dashed lines in Fig. 2 represent the results of these calculations.

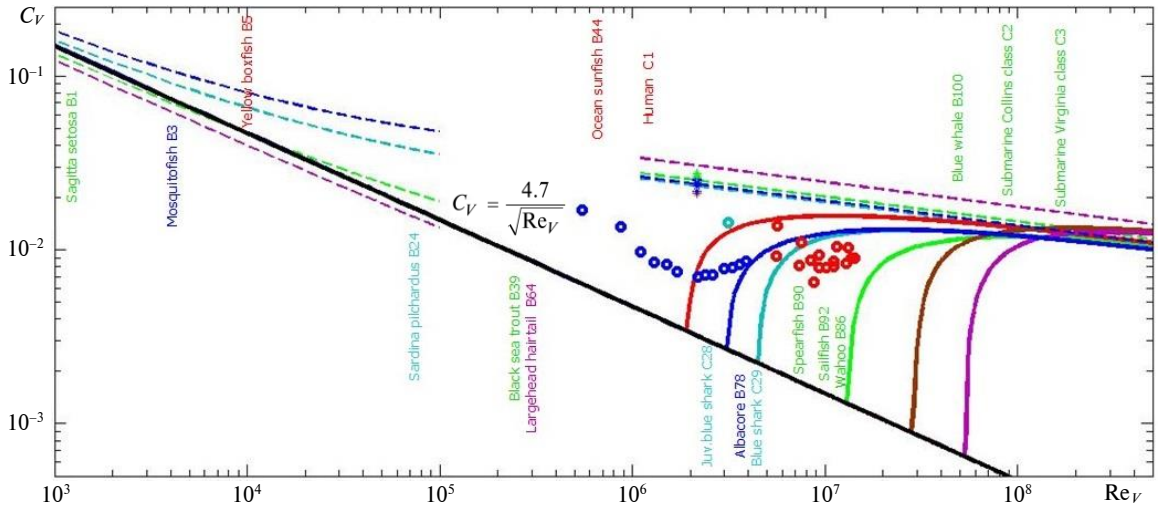

Figure 2: Volumetric drag coefficient versus volumetric Reynolds number for standard (dashed lines) and special shaped (solid lines) bodies of revolution

Laminar (upper dashed lines, (4)) and turbulent (lower dashed lines, (5)) drag coefficients for standard bodies with $L/D = 4.5$ are presented by dashed dark blue lines; $L/D = 5.9$ – blue lines; $L/D = 12.4$ – green lines; $L/D = 33.3$ – magenta lines. Solid lines represent drag estimations for special shaped bodies shown in Fig. 1: unseparated unclosed body UA-2 ($L/D = 3.52$; red line); closed bodies UA-4.5c "Albacore" ($L/D = 4.5$; dark blue line), UA-5.9c "Blue shark" ($L/D = 5.9$; blue line), UA-12.4c "Sailfish" ($L/D = 12.4$; green line), UA-33.3c "Largehead hairtail" ($L/D = 33.3$; magenta line); unclosed body UA-23.3 ($L/D = 23.3$; brown line). Markers show the experimental data for standard ("stars", [17]) and other special shaped bodies of revolution ("circles"): red – "Dolphin" body [2] ($L/D = 3.33$), blue – Goldschmied body [17] ($L/D = 2.9$), dark blue – Hansen&Hoyt body [24] ($L/D = 4.5$). Typical values of volumetric Reynolds numbers calculated in [10] are shown by names

To find the critical Reynolds number for the laminar-to-turbulent transition in the boundary layer on the slender unseparated bodies of revolution, the Tollmin–Schlichting–Lin theory [13] and Mangler–Stepanov transformations [20] were used in [10, 11, 14]. The boundary-layer on a flat plate remains laminar for any frequencies of disturbances, if

$$\mathrm{Re}^* = \frac{\bar{U}\bar{\delta}^*}{\nu} < 420.$$

Taking into account the Blasius expression for displacement thickness [20] $\bar{\delta}^* = 1.721(\bar{x})^{1/2}\,\mathrm{Re}_L^{-1/2}$, this inequality can be rewritten as follows:

$$\sqrt{\bar{x}\,\mathrm{Re}_L} < 244.04.$$

And with the use of (1), the condition for the axisymmetrical boundary-layer to remain laminar can be written as follows [10, 11, 14]:

$$\mathrm{Re}_L \int_0^x R^2(\xi)d\xi < 59558. \qquad (6)$$

If the Reynolds number is small enough and inequality (6) holds on the entire body surface ($x = 1$ in (6)), we can calculate the friction drag according to (2) and obtain formula (3). Otherwise, the boundary layer remains laminar only on the nose part of the body surface (on the interval $0 \le \xi \le x$). For the interval $x \le \xi \le 1$ we can use eq. (5) without the term $7(D/L)^3$, since our bodies are expected to be unseparated. Solid lines in Fig. 2 represent the results of calculations for special shaped bodies of revolution shown in Fig. 1.

Results

Locomotion with the use of attached flow patterns

The power balance for a steady horizontal motion at speed U of an animal or vehicle of weight Mg can be written as follows:

$$q\eta Mg = XU \qquad (7)$$

where q is the power per unit weight used for locomotion; η $(0 \le \eta \le 1)$ is the propulsion efficiency; the hydrodynamic drag X can be expressed with the use of volumetric drag coefficient C_V:

$$X = 0.5C_V\rho U^2 V^{2/3}. \qquad (8)$$

Since values q and η are limited, the maximal speed can be achieved at small drag coefficients, in particular, without any boundary layer separation. The trunks of best swimming animals ensure such attached flow patterns [7, 8].

Table 1: Theoretical estimations of the drag and maximal speed for the laminar and the turbulent axisymmetric unseparated hulls

No.	Characteristic	Laminar flow	Turbulent flow
1	Drag coefficient	$C_V = \frac{4.7}{\sqrt{\mathrm{Re}_V}}$ (9a)	$C_V \approx \mathrm{const} \approx 0.01$ (9b)
2	Maximal speed at constant η	$U = 0.71(q\eta g)^{0.4}\left(\frac{V}{\nu}\right)^{0.2} \sim L^{0.6}$ (10a)	$U = \left(\frac{2q\eta g}{C_V}\right)^{1/3} V^{1/9} \sim L^{1/3}$ (10b)
3	Maximal speed at $C_T >> 1$	$U \sim L^{7/9}$ (13a)	$U \sim L^{1/3}$ (13b)

The theoretical estimations of C_V for laminar and turbulent cases are shown in Table 1 (line 1). Formulas (9a) and (9b) are in good agreement with Hoerner's formula for laminar drag on slender ellipsoids and for the friction drag in developed turbulent flow respectively (see Fig. 2). With the use of assumption of neutral buoyancy ($M = \rho V$), eqs. (7), (8), (9a), and (9b) yield estimations of the maximal speed at fixed values of the propulsion efficiency η (see Table 1, line 2). Formulas (10a), (10b) illustrate that the maximal speed weakly increases with the body or hull length. Both relationships differ from the known linear dependence (e.g., burst swimming corresponds to speeds of circa 10 body lengths per second for sub-carangiform fish of between 10 and 20 cm in length [25]). Later we will try to estimate the speed-to-length dependence with the use of statistical information about water animals (see Tables A, B, and C).

Mechanisms of thrust creating and their efficiency can be very different [26, 27]. To take into account the probable dependence $\eta(L)$, we will use here the theory of ideal propeller [28] and corresponding formula:

$$\eta = \frac{2}{1+\sqrt{1+C_T}}, \; C_T = \frac{2T}{\rho U^2 A_{\mathrm{disc}}} \qquad (11)$$

where $T = X$ is the thrust; A_{disc} is the area of an ideal propeller. At small values of the thrust coefficient C_T, $\eta \to 1$ and formulas (10a) and (10b) can be used. If $C_T >> 1$, eqs. (11) yield

$$\eta = U\sqrt{\frac{2\rho A_{\mathrm{disc}}}{T}}. \qquad (12)$$

For the neutral buoyant case ($M = \rho V$) putting eq. (12) into (7), we obtain:

$$qMg\sqrt{\frac{2\rho A_{\mathrm{disc}}}{T}} = T; \;\; T = \rho(qVg)^{2/3}(2A_{\mathrm{disc}})^{1/3}.$$

Then with the use of (8) and $T = X$:

$$C_V U^2 = 2(2A_{\mathrm{disc}})^{1/3}(qg)^{2/3}.$$

Finally, taking into account (9a) and (9b) and assuming $A_{\mathrm{disc}} \sim L^2$ and $V \sim L^3$ we obtain estimations of the maximal speed for the case of an ideal propeller with $C_T >> 1$ (see Table 1, line 3). In comparison with (10a), dependence (13a) is much closer to the linear one. For the turbulent flow pattern, formulae (10b) and (13b) yield the same weak increase of the speed versus length.

Statistical analysis of the speed-to-length dependence for aquatic animals

If we assume that

$$U = kL^p \qquad (14)$$

(in such dependences we will measure the swimming speed in m/s and body length in m), then $u = \ln k + pl$ ($u = \ln U$, $l = \ln L$). We can treat l and u as random variables and use linear regression, [29], to estimate constant parameters k and p for the aquatic animal locomotion. A similar statistical approach was used in [30] to link animal speeds with tail beat amplitude and frequency. The length and speed values available in the literature and internet are shown in Tables A, B, and C and in Fig. 3. The results of the statistical analysis are presented in Table 2. We have not used the information about flying animals, human swimming, animals with non-slender trunks ($D/L > 0.25$) and with the anguilliform propulsion, in order to check our assumptions about unseparated body shapes and estimations presented in Table 1.

Application of a multiple regression for animals represented in Table B (without whales) yields:

$$U \approx 8.43L^{0.775}(D/L)^{0.113} \qquad (15)$$

(the number of observations $n = 79$; the number of parameters in the regression $m = 3$; the regression

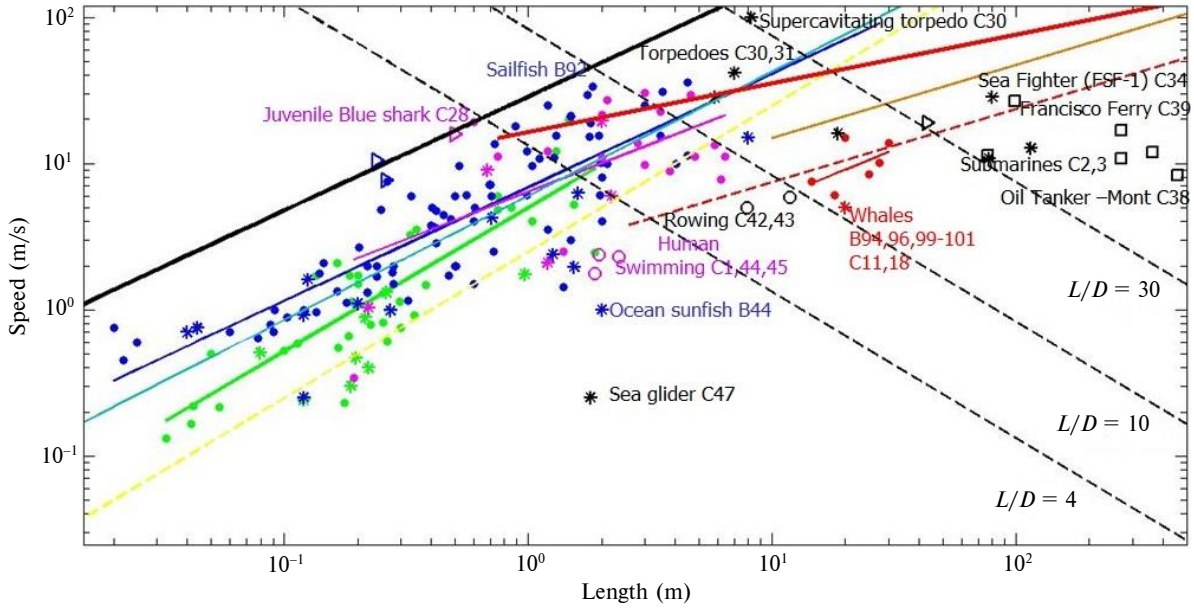

Figure 3: Speed versus length dependences

Animals are shown by green markers for Table A; dark blue markers for B; magenta – for C; red – for whales from tables B and C. "Stars" correspond to the cases $L/D < 4$ or animals with the anguilliform propulsion; "triangles" – to flying animals, "circles" – to human swimming; all these three cases do not participate in the statistical analysis. Black markers represent vehicles ("stars" – underwater or SWATH, "squares" – floating, "circles" – human rowing shells, "triangle" – Hydrofoil craft PTS 150 MK III). Regression results are represented by straight lines (green for Table A; dark blue for B (without whales); magenta for C (without whales); red short line – for whales from tables B and C). Blue line represents the linear regression based on all the animal information from Tables A, B, and C (without whales). Bold black line represents the maximum speed for the laminar flow pattern (eq. (16)); bold red line – for the turbulent one (eq. (21b)). Commercial efficient speeds are shown by dashed yellow and red lines for laminar and turbulent unseparated hulls respectively. Critical speeds for the laminar flow (19) are shown by the black dashed lines for $L/D = 4$, 10, and 30. Brown line represents the critical velocity $U = 4.72\sqrt{L}$

Table 2: The results of statistical analysis for animals represented in Tables A, B, and C

No.	Source of statistical information about animals	Number of observation (animals) n	Correlation coefficient r	Coefficients in eq. (14)		Experimental value of Fisher function $F = \frac{r^2(n-m)}{[(1-r^2)(m-1)]}$, $m = 2$	Critical value of Fisher function for the confidence level 0.01	F/F_c
				p	k			
1	Table A	35	0.865	0.983	5.015	98.09	$F_c(1, 33) = 7.47$	13.1
2	Table B without whales	79	0.843	0.777	6.88	188.46	$F_c(1, 77) = 6.98$	27
3	Table C without whales	18	0.572	0.650	6.41	7.77	$F_c(1, 16) = 8.53$	0.91
4	Total without whales, Tables A, B, and C	132	0.850	0.850	6.01	337.02	$F_c(1, 130) = 6.9$	48.8
5	Whales, Tables B and C	6	0.536	0.682	1.18	9.79	$F_c(1, 4) = 21.2$	0.46

coefficient $r = 0.964$; the value of the Fisher function $F = 493.2$ and its critical value $F_c(2, 76) = 4.9$ at the confidence level 0.01). It can be seen that the most reliable estimations (the highest values of F/F_c) correspond to the animals from Table B (see Table 2, line 2), total data (line 4) and formula (15). The corresponding values of the power coefficient p are very close to the theoretical value 7/9 from eq. (13a). Unfortunately, we do not have enough information about whales to check dependencies (10b), (13b), and (14) (see Table 2, line 5). It must be noted that standard assumption about the drag proportionality $X \sim U^2$ (e.g., it corresponds to the constant volumetric drag coefficient, see eq. (8)) leads to a very weak speed versus length dependence $U \sim L^{1/3}$ (see (10b) and (13b)), which is not supported by animals data.

Estimations of the maximal speed for the laminar flow pattern

Since the dependence $U = kL^{7/9}$ is substantiated both theoretically and statistically, we can use it to estimate the maximal speed in the laminar flow. For this purpose it is enough to find the maximal value of the coefficient k, i.e. the maximum of the ratio $U/L^{7/9}$. The calculations are presented in Tables A, B, and C. It can be seen that the maximal value of this ratio – 28.6 $m^{2/9}/s$ – corresponds to the juvenile Blue shark (C, line 28). Thus, the maximal speed for laminar flow pattern can be estimated from the equation:

$$U_{\max} \approx 28.6 L^{7/9} \tag{16}$$

The black bold line represents dependence (16) in Fig. 3.

Estimations of the commercial efficient speed

Formulae (16) allow us to estimate the maximal speed of animals or well shaped vehicles with effective locomotion, which can be achieved only for short periods of time (in particular, this velocity corresponds for un-aerobic processes in animals). To achieve the maximal range at fixed amount of energy accumulated on board or in body, we need to maximize the weight-to-drag ratio W/X [11, 31]. For neutral buoyancy ($W = Mg = \rho Vg$), formula (8) yields $X/W = 0.5 C_V U^2 V^{-1/3}/g$. Then with the use of (9a), (9b) and the volume estimation for the special shaped closed unseparated bodies of revolution [10]

$$\frac{V}{L^3} = \gamma \left(\frac{D}{L}\right)^2 \tag{17}$$

(with the average value $\gamma = 0.285$), we can calculate the commercial efficient speed for the attached laminar and turbulent cases at different values W/X. The corresponding lines are shown in Fig. 3 by dashed yellow (laminar case) and red (turbulent case) lines for $W/X = 50$; $D/L = 0.1$; $\nu = 10^{-6}$ m^2/s. It can be seen that laminar commercial effective velocities are much lower than the maximal ones, but whale speeds are close to the commercial efficient one. Very small speed of underwater glider (see Fig. 3, Table C, 47) ensures its high commercial efficiency. In Fig. 3, the brown line represents the critical velocity $U = 4.72\sqrt{L}$ corresponding to the drastic increase of the wave drag for ships (vehicles floating on the water surface) [32].

Speed limit for the laminar flow pattern

Formulae (16) demonstrate that speed can increase rather fast with the length of proper shaped laminar unseparated vehicle with effective propulsion. Nevertheless, the use of (16) is limited, since fast and large vehicles (and also animals, e.g., whales) cannot ensure a laminar boundary layer on the entire surface. The corresponding critical Reynolds number was estimated in [10, 11, 14]:

$$\mathrm{Re}_L^* = \frac{UL}{\nu} = \frac{59558\pi L^3}{V}. \tag{18}$$

Eqs. (17) and (18) show that slenderer bodies ensure higher values of the critical Reynolds number (see also [10, 11, 14] and points of bifurcation in Fig. 2). Taking into account (17) and (18) the critical velocity can be found:

$$U^* = 6.34 \cdot 10^5 \frac{\nu}{L}\left(\frac{L}{D}\right)^2 \tag{19}$$

(for $\gamma = 0.285$). At lower speeds a slender special shaped unseparated body of revolution ensures the laminar boundary layer. Dependences (19) are shown in Fig. 3 by black dashed lines for different values of the aspect ratio L/D and $\nu = 1.3 \cdot 10^{-6}$. Putting (16) into (19), we obtain $U_{\max} < U^*_{\max}$, where

$$U^*_{\max} = 2312 \nu^{7/16} (L/D)^{7/8}. \tag{20}$$

Relationship (20) demonstrates that the maximal possible velocity with the pure laminar flow pattern is independent on length and that the increase

of the aspect ratio L/D allows increasing the vehicle speed. In particular, for $L/D > 28$, a vehicle with a special shaped unseparated hull could exceed the speed 100 m/s.

Eq. (20) was used to calculate the maximum possible speed for the pure laminar flow pattern at $\nu = 1.3 \cdot 10^{-6}$ m^2/s. The results are shown in Tables B and C. Since all the analysis is valid for $L/D \geq 4$, eq. (20) yields $U^*_{\max} \geq 20.7$ m/s. Thus all the velocities in Table A are lower than $U^*_{\max}$. The same is valid for the animal data presented in Table C. In Table B there are only three exceptions: Atlantic bluefin tuna, Swordfish and Black marlin (lines 93, 95, and 98).

Maximal speed for the turbulent flow pattern

For the developed turbulent flow, we can estimate the maximal speed with the use of (9b), (10b) and the highest value the capacity-efficiency $C_E = q\eta$ [10, 11]. According to the data presented in Table C, the maximum $C_E = q\eta = 8.5$ m/s corresponds to the juvenile Blue shark (C-28), see also [11]. Then

$$U_{\max} \approx 25.5V^{1/9} \approx 22.3L^{1/3}(D/L)^{2/9}; \quad U^*_{\max} \approx 16.4L^{1/3}. \qquad (21a, b)$$

Eq. (21a) demonstrates that the maximal possible velocity weakly increases with the length and diminishes with the increase of the aspect ratio. Since our analysis is not valid at $D/L > 0.25$, we used $D/L = 0.25$ to obtain the maximal possible value of speed (eq. (21b)) and to show it in Fig. 3 by the bold red line. For Swordfish and Black marlin (B-95, 98) formula (21a) yields values 23.5 and 25.2 m/s respectively which are much smaller than presented in Table B and estimation (20).

Discussion

High-speed underwater options: attached flow or supercavitation

High speeds can cause cavitation in water, since the local pressures and cavitation number

$$\sigma = \frac{2g(h+10)}{U^2} \qquad (22)$$

decrease (here we neglected the pressure inside the cavity in comparison with the atmospheric pressure, corresponding to the water column of 10 m, h is the depth of steady motion in meters). The simplest way to estimate the critical speed of the cavitation inception U^*_C is to put in (22) $\sigma = -C_P^{(\min)}$ [33, 34], where $C_P^{(\min)}$ is the minimum value of the pressure coefficient on the vehicle surface. Dependences $U^*_C(h)$ are shown in Fig. 4 for special shaped bodies of revolution presented in Fig. 1. It can be seen that animal velocities presented in Tables A, B and C do not exceed the corresponding values for cavitation inception on their trunks. This issue, as well as the cavitation inception on fish fins, was discussed in [35].

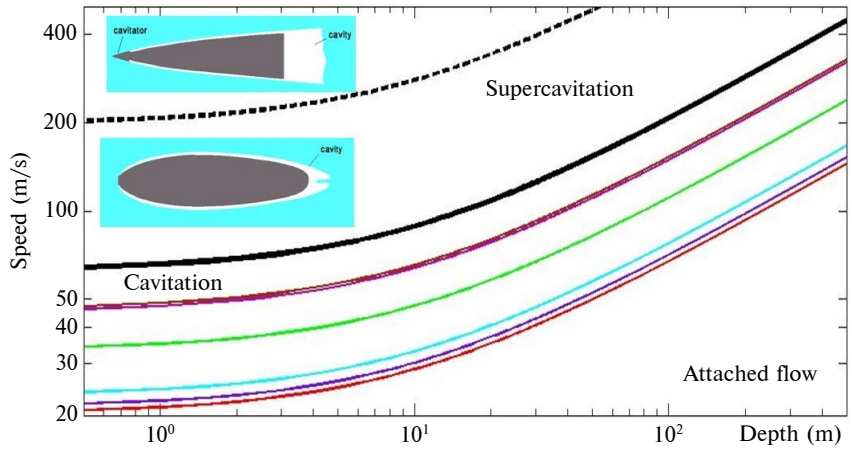

Figure 4: Critical speeds U^*_C, U^*_T and U^*_L in m/s versus the depth of steady horizontal motion h in meters

Critical speed of cavitation inception U^*_C for different bodies: UA-2 ($L/D = 3.52$; red line); UA-4.5c "Albacore" ($L/D = 4.5$; dark blue line); UA-5.9c "Blue shark" ($L/D = 5.9$; blue line); UA-12.4c "Sailfish" ($L/D = 12.4$; green line); UA-33.3c "Largehead hairtail" ($L/D = 33.3$; magenta line); UA-23.3 ($L/D = 23.3$; brown line). Black solid and dashed lines represent critical speeds U^*_T and U^*_L respectively

Decreasing the cavitation number leads to the formation of large enough supercavities, which can cover hulls and thereby reduce the friction drag (see Fig. 4 and [36–38]). For the disc cavitator (a part of the hull wetted by water) and when the entire cavity volume is used to locate the hull (as shown in lower pictogram in Fig. 4), the volumetric pressure drag coefficient can be estimated as follows [37]:

$$C_{VP} = \frac{2X_P}{\rho U^2 V^{2/3}} = \sqrt[3]{\frac{9\pi\sigma^4}{-16\ln\sigma}} \approx C_V \qquad (23)$$

(X_P is a pressure drag). Formula (23) illustrates that $C_V < 0.01$ at $\sigma < 0.05$. The same estimations are valid for slender cavitators [37], i.e. we can have smaller drag than on unseparated hulls of the same volume with the turbulent boundary layer (see (10b)). The corresponding critical speed U_T^* is calculated by putting into (22) $\sigma = 0.05$ and shown in Fig. 4 by the solid black line.

Eq. (23) demonstrates that approximate dependencies are valid: $C_V \sim \sigma^{4/3} \sim U^{-8/3}$ (according to (22)) and $X \sim U^{-2/3}$ (according to (8)). It means that drag on supercavitating vehicles reduces with the increase of speed (when the hull volume is fixed, but its shape changes to be located in the corresponding cavity). This much unexpected conclusion was also confirmed by the results given in [38] for sub- and supersonic speeds.

The supercavitating hulls using the cavity volume completely (see lower pictogram in Fig. 4) must have the aspect ratio L/D coinciding with the λ for the cavity, which increases with the diminishing of the cavitation number approximately as $\lambda \sim 1/\sqrt{\sigma}$ [39]. Since the strength and stability of rigid hulls cannot be ensured at very large L/D values, the applications of the supercavitating flow pattern shown in lower pictogram and formula (23) is limited.

It is possible to use only the nose part of the cavity in order to locate the hull with a fixed value of λ as shown in upper pictogram. The corresponding values of C_V are larger than (23) but small enough to ensure high speeds of supercavitating vehicles (see details in [37]). In particular, $C_V < 5\cdot 10^{-4}$ at $\sigma < 0.005$ for hulls with $\lambda > 20$. Thus, the supercavitating flow pattern can ensure the lower drag in comparison with the slender special shaped unseparated bodies (e.g., shown in Fig. 1) with a laminar boundary layer (see Fig. 2). The corresponding critical speed U_L^* is calculated by putting into (22) $\sigma = 0.005$ and shown in Fig. 4 by the dashed black line.

In the velocity region $U_T^* < U < U_L^*$, the advantages of the laminar unseparated hulls over supercavitating ones are limited by two circumstances. First, the length and the volume of the laminar unseparated hulls are limited (see (19) and black dashed lines in Fig. 3). Second, corresponding speeds exceed U_C^* and the problem of cavitation inception must be solved. Probably, unseparated shapes can delay also the cavitation inception. Some theoretical considerations are available in [33, 40]. Experiments presented in [41, 42] demonstrate that cavitation started at the region of the boundary layer separation.

Speed limitations for supercavitation

Supercavitation requires compensation of the vehicle weight since its hull moves in gas (as in the case of aircraft, see Fig. 4). It can be implemented by using wings or by hull planning on the cavity surface (with the lift force $Y_W = W$). Corresponding additional drag X_W limits the advantages of supercavitation [37]. In particular, the additional capacity-efficiency [11]:

$$\Delta(q\eta) = U/k_W, \quad k_W = Y_W/X_W \qquad (24)$$

increases linearly with the speed and exceeds the estimation $C_E = q\eta = 8.5$ m/s (juvenile Blue shark) at $U > 200$ m/s and $k_W < 23.5$. Modern supersonic aircrafts use fuels with high values of the specific impulse q and may have much higher capacity-efficiency. In particular, the C_E value of Lockheed SR-71 Blackbird (the fastest air breathing aircraft [43]) can be estimated as 253 m/s (cruising speed 917 m/s, $X/W = T/W = 3.6$). Taking this value as a maximum possible for modern technologies, we can use (7), (8), and (24) to estimate the maximum speeds of supercavitating vehicles

$$q\eta = \frac{C_V U^3}{2g\bar{\rho}V^{1/3}} + \frac{U}{k_W} < 253 \text{ m/s}, \quad \bar{\rho} = \frac{M}{\rho V}. \qquad (25)$$

Inequality (25) demonstrates that faster vehicles must have smaller values of drag coefficient C_V and larger values of the volume, the average density coefficient $\bar{\rho}$ and weight-to-drag ratio.

Let us estimate capacity-efficiency of supercavitation at $V = 1$ m^3, $k_w = 10$, $\bar{\rho} = 3$, $h = 5$ m for two different speeds: 250 m/s and 1000 m/s. Corresponding values of the cavitation number are 0.0047 and 0.00029 (see (22)), and $C_V \approx 5\cdot 10^{-4}$ and $C_V \approx 10^{-4}$ (see [37]) respectively. Then eq. (25)

yields $q\eta \approx 158$ m/s and $q\eta \approx 1800$ m/s respectively. It can be seen that inequality (25) does not hold at higher speed 1000 m/s, but it is possible to achieve this speed for large vehicles with $V > 1500$ m^3. Thus, the idea of a superfast supercavitating submarine does not look utopian [38].

Conclusions

As shown by theoretical and statistical analysis, the perfect body shapes of most aquatic animals provide an attached laminar flow pattern. The swimming speed of these animals is proportional to the length of the body in power 7/9. The exception is whale locomotion that occurs in turbulent mode at supercritical Reynolds numbers.

Estimated maximum speeds for laminar and turbulent flow patterns show that the special shaped unseparated hulls can greatly increase the speed of underwater vehicles and SWATH ships. Further increase in speed of underwater motion can be achieved with the use of supercavitating hulls and greater than animal capacity-efficiency.

Acknowledgements

I would like to express my sincere thanks to professors Alberto Redaelli, Giuseppe Passoni and Gianfranco Fiore (Politecnico di Milano), Rolf Radespiel and Dirk Langemann (TU Braunschweig) and Juergen Prestin (University of Luebeck) for their support and interesting discussions.

References

[1] Gray J. Studies in animal locomotion VI. The propulsive powers of the dolphin. J Exp Biol. 1936;13:192-9.
[2] Greiner L, editor. Underwater missile propulsion. Arlington: Compass Publications; 1967.
[3] Fish FE, Rohr J. Review of dolphin hydrodynamics and swimming performance. San Diego: SPAWARS, 1999. Technical report 1801.
[4] Fish FE. The myth and reality of Gray's paradox: implication of dolphin drag reduction for technology. Bioinspiration Biomimetics. 2006;1:R17-R25. DOI: 10.1088/1748-3182/1/2/r01
[5] Fish FE, Legac P, Williams TM, Wei T. Measurement of hydrodynamic force generation by swimming dolphins using bubble DPIV. J Exp Biol. 2014;217:252-60. DOI: 10.1242/jeb.087924
[6] Bale R, Hao M, Bhalla AP, Patel N, Patankar NA. Gray's paradox: A fluid mechanical perspective. Sci Rep. 2014;4:5904. DOI: 10.1038/srep05904
[7] Aleyev YuG. Nekton. W Junk, The Hague; 1977.
[8] Rohr J, Latz MI, Fallon S, Nauen JC, Hendricks E. Experimental approaches towards interpreting dolphin stimulated bioluminescence. J Exp Biol. 1998;201:1447-60.
[9] Nesteruk I. Rigid bodies without boundary-layer separation. Int J Fluid Mech Res. 2014;41(3):260-81. DOI: 10.1615/interjfluidmechres.v41.i3.50
[10] Nesteruk I, Passoni G, Redaelli A. Shape of aquatic animals and their swimming efficiency. J Marine Biol. 2014;2014:470715. DOI: 10.1155/2014/470715
[11] Nesteruk I. Efficiency of steady motion and its improvement with the use of unseparated and supercavitating flow patterns. Naukovi Visti NTUU KPI. 2016;6:51-67. DOI: 10.20535/1810-0546.2016.6.81605
[12] Nesteruk I, Brühl M, Möller T. Testing a special shaped body of revolution similar to dolphins trunk. Naukovi Visti NTUU KPI. 2018;2:44-53. DOI: 10.20535/1810-0546.2018.2.129140
[13] Landau LD, Lifshits EM. Fluid mechanics. 2nd ed. Butterworth-Heinemann; 1987. Volume 6. Course of theoretical physics.
[14] Nesteruk I. Peculiarities of turbulization and separation of boundary-layer on slender axisymmetric subsonic bodies. Naukovi Visti NTUU KPI. 2002;3:70-6.
[15] Nesteruk I. Body forms of minimal drag. Dopovidi AN USSR Ser A. 1989;4:57-60.
[16] Lutz T, Wagner S. Drag reduction and shape optimization of airship bodies. J Aircraft. 1998;35(3):345-51. DOI: 10.2514/2.2313
[17] Goldschmied FR. Integrated hull design, boundary layer control and propulsion of submerged bodies: Wind tunnel verification. In: AIAA (82-1204). Proceedings of the AIAA/SAE/ASME 18th Joint Propulsion Conference. 1982. p. 3-18. DOI: 10.2514/6.1982-1204
[18] Nesteruk I. Experimental investigation of axisymmetric bodies with negative pressure gradients. Aeronaut J. 2000;104:439-43.
[19] Babenko VV, Carpenter PW. Dolphin hydrodynamics. In: Carpenter PW, Pedley TJ, editors. Flow past highly compliant boundaries and in collapsible tubes. Fluid mechanics and its applications. Dordrecht: Springer; 2003. DOI: 10.1007/978-94-017-0415-1_13
[20] Loitsyanskiy LG. Mechanics of liquids and gases. 6th ed. New York, Wallingford: Begell House; 1995. 961 p.
[21] Cole JD. Perturbation methods in applied mathematics. Waltham, London: Blaisdell Pub. Co.; 1968.
[22] Nesteruk I. Reserves of the hydrodynamical drag reduction for axisymmetric bodies. Bulletin of Kiev University Ser Phys Math. 2002;1:112-8.
[23] Hoerner SF. Fluid-dynamic drag. Midland Park, N.J.; 1965.

[24] Hansen RJ, Hoyt JG. Laminar-to-turbulent transition on a body of revolution with an extended favorable pressure gradient forebody. J Fluids Eng. 1984;106:202-10. DOI: 10.1115/1.3243103
[25] Bainbridge R. Speed and stamina in three fish. J Exp Biol. 1960;37:129-53.
[26] Lighthill MJ. Note on the swimming of slender fish. J Fluid Mech. 1960;9:305-17. DOI: 10.1017/s0022112060001110
[27] Webb PW. Hydrodynamics and energetics of fish propulsion. Bull Fish Res Board Can. 1975;190:1-159.
[28] Spakovszky ZS. 11.7.4.5 Typical propeller performance. In: MIT turbines; 2002. 16.Unified: Thermodynamics and Propulsion.
[29] Draper NR, Smith H. Applied regression analysis. 3rd ed. John Wiley; 1998.
[30] Gazzola M, Argentina M, Mahadevan L. Scaling macroscopic aquatic locomotion. Nature Phys. 2014;10:758-61. DOI: 10.1038/nphys3078
[31] Gabrielly Y, Von Karman T. What price speed. Mech Eng. 1950;72(10):775-9.
[32] Wave-making resistance [Internet]. En.wikipedia.org. 2019 [cited 2019 Apr 24]. Available from: https://en.wikipedia.org/wiki/Wave-making_resistance
[33] Knapp RT, Daily JW, Hammitt FG. Cavitation. New York: McGraw Hill; 1970.
[34] Franc JP, Michel JM. Fundamentals of cavitation. Dordrecht: Kluwer; 2004.
[35] Iosilevskii G, Weihs D. Speed limits on swimming of fishes and cetaceans. J R Soc Interf. 2008 Mar 6;5(20):329-38. DOI: 10.1098/rsif.2007.1073
[36] Logvinovich GV. Hydrodynamics of flows with free boundaries. Kyiv: Naukova Dumka; 1969.
[37] Nesteruk I., editor. Supercavitation. Advances and perspectives. Springer; 2012.
[38] Nesteruk I. Drag drop on high-speed supercavitating vehicles and supersonic submarines. Appl Hydromech. 2015;17(4):52-7. Available from: http://hydromech.org.ua/content/pdf/ph/ph-17-4%2852-57%29.pdf
[39] Garabedian PR. Calculation of axially symmetric cavities and jets. Pac J Math. 1956;6(4):611-84. DOI: 10.2140/pjm.1956.6.611
[40] Nesteruk I. Can shapes with negative pressure gradients prevent cavitation. In: Proceedings of FEDSM'03, 4th ASME_JSME Joint Fluids Engineering Conference; 2003; Honolulu, USA. Paper number FEDSM2003-45323.
[41] Takahashi S, Washio S, Uemura K, Okazaki A. Experimental study on cavitation starting at and flow characteristics close to the point of separation. In: 5th Symposium on cavitation; 2003. No. Cav03-OS-3-003.
[42] Washio S. Recent developments in cavitation mechanisms. A guide for scientists and engineers. Woodhead Publishing; 2014. 256 p.
[43] Lockheed SR-71 Blackbird [Internet]. En.wikipedia.org. 2019 [cited 2019 Apr 24]. Available from: https://en.wikipedia.org/wiki/Lockheed_SR-71_Blackbird.
[44] Bainbridge R. The speed of swimming of fish as related to size and to the frequency and amplitude of the tail beat. J Exp Biol. 1958;35:109-33.
[45] Bottlenose Dolphin | Speed of Animals [Internet]. Speedofanimals.com. 2019 [cited 2019 Apr 24]. Available from: http://www.speedofanimals.com/animals/bottlenose_dolphin

Supplementary tables

Table A: Fish data extracted from [44] and calculations

Body lengths were calculated with the use of speed and U/L data presented in [44]. The data corresponding to jumping are eliminated. "Non-slender" animals (with $D/L > 0.25$) are labeled by "star" and are not used in statistical analysis

No.	Name	Primal information		Calculations	
		Speed U (m/s)	Ratio U/L (s^{-1})	Body length L (m)	$U/L^{7/9}$ ($m^{2/9}/s$)
1	*2*	*3*	*4*	*5*	*6*
1	Carp	0.59	5.2	0.113	3.21
2	Carp	0.52	5.2	0.100	3.12
3	Carp	0.22	5.2	0.042	2.57
4	Bleak	0.50	10.0	0.050	5.14
5	Chub*	0.24	2.0	0.120	1.25
6	Sea trout	0.92	2.7	0.341	2.13
7	Mackerel	0.81	3.2	0.250	2.36
8	Twaite shad	0.75	2.5	0.300	1.91
9	Perch	0.66	3.6	0.183	2.47
10	Meagre	1.13	3.8	0.297	2.90
11	Whiting	0.23	1.3	0.177	0.88
12	Bib or Pout	0.55	3.3	0.167	2.22

Table A continuation

1	*2*	*3*	*4*	*5*	*6*
13	Grey mullet	0.61	2.3	0.265	1.71
14	Rudd	1.14	6.0	0.190	4.15
15	Lesser Weever*	0.40	1.8	0.222	1.29
16	Hake	0.79	3.5	0.226	2.51
17	Pike	1.48	3.9	0.379	3.14
18	John Dory*	0.30	1.6	0.188	1.10
19	Trout	3.50	10.0	0.350	7.92
20	Salmon	4.79	6.4	0.748	6.00
21	Salmon	4.95	5.8	0.853	5.60
22	Salmon	6.00	8.0	0.750	7.50
23	Tuna	19.67	13.4	1.468	14.59
24	Gold fish*	0.51	6.4	0.080	3.63
25	Salmon	0.22	4.0	0.054	2.09
26	Salmon	0.17	4.0	0.042	1.97
27	Salmon	0.13	4.0	0.032	1.87
28	Southern ground shark	5.21	3.4	1.533	3.74
29	Southern ground shark	4.05	3.9	1.039	3.93
30	Spotted jewfish*	1.74	1.8	0.965	1.79
31	Lemon shark	2.44	1.3	1.876	1.49
32	Barracuda	12.19	9.4	1.300	9.96
33	Pike	2.10	12.7	0.165	8.51
34	Pike	1.50	7.5	0.200	5.24
35	Carp	1.70	12.6	0.135	8.07
36	Rudd	1.30	5.9	0.220	4.22
37	Dace	1.70	9.2	0.185	6.32
38	Red gurnard	0.47	2.4	0.196	1.67
39	Black bass	0.88	4.1	0.215	2.91
40	Gurnard*	1.31	5.0	0.262	3.71
41	Norway haddock*	0.98	3.6	0.272	2.70
42	Western sucker*	3.23	9.8	0.330	7.66
43	Rainbow trout	1.70	8.5	0.200	5.94

Table B: Water animal data presented in Aleyev's book [7] and calculations

Speed values are extracted form Reynolds number data presented in [7] and $\nu = 1.3 \cdot 10^{-6}$ m^2/s, corresponding to the water temperature approximately 10 °C. Unfortunately, there is no information in [7] which value of viscosity was used to calculate the Reynolds number. The whales are marked in red; their statistical analysis was carried out separately. Flying animals are marked in blue, animals with the anguilliform propulsion – in yellow. Their data and "Non-slender" animals (with $D/L > 0.25$) are not used in statistical analysis. Corresponding species are labeled by "star". Speeds exceeding the estimation (20) are shown in magenta

No.	Species	Primal information			Calculations	
		Body length L (cm)	Speed U (m/s)	Ratio D/L	$U/L^{7/9}$ ($m^{2/9}/s$)	$U^*_{\max}$ Eq. (20)
1	*2*	*3*	*4*	*5*	*6*	*7*
1	*Sagitta setosa* Muell	2.2	0.40	0.06	8.76	71.2
2	*Lebistes reticulates* Peters	2.5	0.60	0.23	10.57	22.2
3	*Gambusia affinis holbrooki* Girarb	2.0	0.75	0.20	15.72	25.1
4	*Xiphophorus maculatus* Guenth*	4.0	0.70	0.28	8.56	18.7
5	*Ostracion tuberculatus* L.*	12.0	0.25	0.34	1.30	15.8
6	*Mollienisia velifera* Reg.*	4.4	0.75	0.29	8.51	18.2
7	*Leucaspius delineatus* Heck	6.0	0.70	0.17	6.24	29.0
8	*Clupeonella delicatula delicatula* Nordm.	7.8	0.64	0.16	4.65	30.6
9	*Glasterosteus aculeatus* L.	9.0	0.70	0.20	4.55	25.1
10	*Xiphophorus helleru* Heck.	8.8	0.79	0.22	5.23	23.1
11	*Gymnammodytes cicerellus* Raf.	10.3	0.88	0.07	5.16	63.0
12	*Atherina bonapartei* Boulenger	9.1	0.99	0.14	6.39	34.3
13	*Chaetodon striatus* L.*	12.0	0.92	0.27	4.79	19.3
14	*Atherina mochon pontica* Eichw.	12.2	0.98	0.14	5.03	34.4

Table B continuation

1	*2*	*3*	*4*	*5*	*6*	*7*
15	*Sprattus sprattus phalericus* Risso	12.0	1.0	0.12	5.20	39.3
16	*Atherina hepsetus* L.	13.5	0.96	0.13	4.56	36.7
17	*Carassius auratis* L.*	12.5	1.60	0.28	8.06	18.7
18	*Spicara smaris* L.	18.0	1.11	0.22	4.21	23.1
19	*Carassius carassius* L.*	20.0	1.10	0.28	3.85	18.7
20	*Alosa caspia nordmanni* Antipa	16.5	1.33	0.16	5.40	30.6
21	*Engraulis encrasicholus ponticus* Alex	14.0	1.78	0.16	8.21	30.6
22	*Zeus faber pungio* Val.*	27.3	0.99	0.27	2.72	19.3
23	*Scardinius erythrophthalmus* L.	22.0	1.32	0.22	4.29	23.1
24	*Sardina pilchardus* Walb.	14.5	2.07	0.17	9.29	29.0
25	*Labrus viridis* L.	32.1	1.15	0.21	2.78	24.1
26	*Perca fluviatilis* L.	24.0	1.67	0.22	5.07	23.1
27	*Sciaena umbra* L.	28.0	1.50	0.22	4.04	23.1
28	*Serranus scriba* L.	22.0	2.00	0.20	6.49	25.1
29	*Rutilus rutilus* L.	24.0	2.00	0.20	6.07	25.1
30	*Alosa kessleri pontica* Eichw.	27.9	1.79	0.16	4.83	30.6
31	*Leuciscus leuciscus* L.	20.2	2.68	0.18	9.30	27.6
32	*Clupea harengus pallasi* Val.	28.0	2.00	0.17	5.38	29.0
33	*Odontogadus merlangus euxinus* Nordm.	47.1	1.70	0.18	3.05	27.6
34	*Abramis brama* L.	60.0	1.50	0.23	2.23	22.2
35	*Cyprinus carpio carpio* L.	50.0	2.00	0.21	3.43	24.1
36	*Belone belone euxini* Günth.	50.4	1.98	0.05	3.37	84.6
37	*Enhybrina schistosa* Daud.*	90.0	1.22	0.03	1.32	132.2
38	*Umbrina cirrosa* L.	42.0	2.85	0.22	5.60	23.1
39	*Salmo trutta labrax m. fario* L.	25.0	4.80	0.15	14.11	32.3
40	*Anguilla anguilla* L.*	100.8	1.48	0.05	1.47	84.6
41	*Mugil auratus* Risso	41.4	3.62	0.19	7.19	26.3
42	*Mugil saliens* Risso	40.0	3.75	0.18	7.65	27.6
43	*Gadus morhua macrocephalus* Til.	72.0	2.50	0.18	3.23	27.6
44	*Mola mola* L.*	200.0	1.00	0.30	0.58	17.6
45	*Loligo vulgaris* Lam.	26.5	7.55	0.14	21.21	34.4
46	Todarodes sagittatus Lam.	48.3	4.14	0.14	7.29	34.4
47	*Symplectoteuthis oualaniensis* Less.	45.2	4.42	0.14	8.20	34.4
48	*Todarodes pacificus* Steenst.	40.2	4.98	0.11	10.12	42.4
49	*Loligo forbesi* Steenst.	33.3	6.01	0.14	14.14	34.4
50	*Illex coindeti* Vérany*	26.1	7.66	0.12	21.77	39.3
51	*Acipencer stellatus* Pall.	140.0	1.43	0.12	1.10	39.3
52	*Sphyraena sphyraena* L.	42.1	4.75	0.10	9.31	46.1
53	*Stizostedion lucioperca* L.	60.0	4.0	0.17	5.95	29.0
54	*Hirundichthys rondeletii* Cuv. et Val.*	24.0	10.42	0.14	31.62	34.4
55	*Chelonia mydas* L.*	154	1.95	0.30	1.39	17.6
56	*Eretmochelys imbricata* L.*	71.0	4.22	0.33	5.51	16.2
57	*Caretta caretta* L.*	126	2.38	0.37	1.99	14.7
58	*Salmo trutta* L.	60.5	4.96	0.17	7.33	29.0
59	*Scomber scombrus* L.	50.0	6.0	0.18	10.29	27.6
60	*Trachurus mediterraneus ponticus* Aleev	56.0	6.07	0.18	9.53	27.6
61	*Mugil cephalus* L.	70.5	5.95	0.20	7.81	25.1
62	*Squalus acanthias* L.	120	3.50	0.14	3.04	34.3
63	*Acipenser gueldenstaedti colchicus* V. Marti	150	3.0	0.16	2.19	30.6
64	*Trichiurus lepturus* L.	150	3.0	0.03	2.19	132.2
65	*Pygoscelis adeliae* Hombron and Jacquinot	70.0	7.15	0.23	9.44	22.2
66	*Eudyptes chrysolophus* Brandt	69.6	7.18	0.24	9.52	21.4
67	*Auxis thazard* Lac.	52.1	9.60	0.20	15.94	25.1
68	*Pomatomus saltatrix* L.	99.0	6.06	0.17	6.11	29.0
69	*Huso huso* L.	200	4.00	0.17	2.33	29.0
70	*Dermochelys coriacea* L.*	160	6.25	0.32	4.34	16.7
71	*Esox lucius* L.	103.4	9.67	0.14	9.42	34.4
72	*Sarda sarda* Bl.	73.2	13.66	0.20	17.41	25.1

Table B continuation

1	*2*	*3*	*4*	*5*	*6*	*7*
73	*Pagophoca groenlandica* Erxl.	197	6.09	0.22	3.59	23.1
74	*Salmo salar* L.	111.5	10.76	0.19	9.89	26.1
75	*Salmo trutta labrax* Pall.	98.8	12.15	0.17	12.26	29.0
76	*Phocoena phocoena* L.	128	10.94	0.21	9.03	24.1
77	*Arctoceptalus pusillus* Schreb.	200	8.00	0.19	4.67	26.3
78	*Thunnus alalunga* Bonnat.	89.0	17.98	0.22	19.69	23.1
79	*Sphyraena barracuda* Walb.	130	15.38	0.13	12.54	36.7
80	*Sphyrna zygaena* L.	199	10.05	0.16	5.88	30.6
81	*Stenopterygius quadriscissus* Quenst.	210	10.0	0.19	5.61	26.3
82	*Dephinus delphis ponticus* Barab.	178.5	15.12	0.21	9.63	24.1
83	*Scomberomorus commersoni* Lac.	120	25.0	0.15	21.69	32.3
84	*Thunnus obesus* Lowe	195	15.38	0.25	9.15	20.7
85	*Thunnus albacora* Lowe	150	20.67	0.21	15.08	24.1
86	*Acanthocybium solandri* Cuv. et Val.	150	21.33	0.12	15.56	39.3
87	*Coryphaena hippurus* L.	181	18.78	0.16	11.84	30.7
88	*Prionace glauca* L.	403	9.92	0.17	3.35	30.0
89	*Globicephalus melas* Traill	450	11.33	0.21	3.52	24.1
90	*Tetrapturus belone* Raf.	175.5	29.63	0.08	19.13	56.1
91	*Tursiops truncatus* Montagu	350	15.43	0.20	5.82	25.1
92	*Istiophorus platypterus* Show and Nodder	183	33.33	0.10	20.83	46.1
93	*Thunnus thynnus* L.	300	25.0	0.23	10.64	22.2
94	*Balaena mysticetus* L.*	2000	5.00	0.27	0.49	19.3
95	*Xiphias gladius* L.	356	30.90	0.19	11.51	26.3
96	*Physeter catodon* L.	1800	6.11	0.19	0.65	26.3
97	*Orcinus orca* L.*	800	15.0	0.26	2.98	20.0
98	*Makaira indica* Cuv et Val.	450	35.55	0.18	11.04	27.6
99	*Balaenoptera physalus* L.	2500	8.40	0.16	0.69	30.6
100	*Balaenoptera musculus* L.	2750	10.18	0.17	0.77	29.0
101	*Balaenoptera borealis* Less	2000	15.0	0.15	1.46	32.3

Table C: Animal and vehicle data available in internet and calculations

For animals the speed and length values are mostly extracted from [45]; D/L – from [7]; for Swordfish and Black marline their rostrum is taken into account to calculate D/L (neglected in [7]). The same information was used in [11]. The whales are marked in red; their statistical analysis was carried out separately. Flying fish is marked in blue, eel (with the anguilliform propulsion) – in yellow, human sport activity – in magenta. Their data and "non-slender" animals (with $D/L > 0.25$) are not used in statistical analysis. Corresponding species are labeled by "star". The vehicles are labeled by "double star". The maximal value of $U/L^{7/9}$ is marked in green

No.	Name	Primal information			Calculations	
		Length L (m)	Speed U (m/s)	Ratio D/L	$U/L^{7/9}$ ($m^{2/9}/s$)	$U^*_{\max}$ Eq. (20)
1	*2*	*3*	*4*	*5*	*6*	*7*
1	Human (dolphin kick)*	2.34	2.30	0.20	1.19	25.1
2	Submarine Collins class (diesel-electric)**	77.42	10.83	0.10	0.37	46.1
3	Submarine Virginia class (nuclear)**	115.0	12.78	0.09	0.32	50.6
4	Great white shark	6.40	11.11	0.20	2.62	25.1
5	Green jack*	0.22	1.03	0.31	3.33	17.1
6	Juvenile Shortnose sturgeon	0.19	0.34	0.14	1.22	34.4
7	Bottlenose dolphin	3.0	9.72	0.21	4.14	24.1
8	American eel*	1.0	1.08	0.05	1.08	84. 6
9	Barracuda	1.20	12.20	0.17	10.59	29.0
10	Blue whale	30.0	13.90	0.17	0.99	29.0
11	Bluefin tuna*	2.0	19.40	0.26	11.32	20.0
12	California sea lion*	2.20	6.00	0.28	3.25	18.7
13	Chinstrap penguin*	0.68	8.97	0.32	12.11	16.7
14	Common octopus	0.75	11.10	0.17	13.88	29. 0
15	Emperior penguin*	1.20	2.08	0.33	1.81	16.2

Table C continuation

1	*2*	*3*	*4*	*5*	*6*	*7*
16	Flying fish (*Cypselurus californicus*)*	0.50	15.69	0.13	26.90	36.6
17	Great white shark	4.80	11.11	0.20	3.28	25.1
18	Humpback whale	14.50	7.50	0.19	0.94	26.3
19	Killer whale	5.80	13.42	0.23	3.42	22.2
20	Mako shark	2.80	13.90	0.21	6.24	24.1
21	Sailfish (*platypterus*)	3.00	30.56	0.10	13.00	46.1
22	Sea otter	1.40	2.50	0.25	1.92	20.7
23	Striped marlin	3.50	22.50	0.15	8.49	32.3
24	Swordfish (*D*/*L* with rostrum)	2.10	26.90	0.15	15.11	32.3
25	Tiger shark	3.80	8.89	0.19	3.15	26.3
26	Wahoo	2.00	21.40	0.12	12.48	39.3
27	Saltwater Crocodile	6.17	7.80	0.10	1.89	46.1
28	Juvenile Blue shark	0.60	19.20	0.18	28.57	27.6
29	Blue shark (adult)	2.00	10.94	0.18	6.38	27.6
30	Supercavitating torpedo "Shkval"**	8.20	100.0	0.07	19.46	63.0
31	Torpedo Mark 48**	5.79	28.34	0.09	7.23	50.6
32	Torpedo Spearfish**	7.00	41.67	0.08	9.17	56.1
33	GHOST SWATH ship**	18.60	16.00	0.07	1.65	63.0
34	Sea Fighter (FSF-1) (SWATH)**	79.90	28.33	0.05	0.92	84.6
35	USS Wisconsin **	270.0	16.90	0.12	0.22	39.3
36	"Titanic" **	269.1	10.80	0.10	0.14	46.1
37	Clipper "Sovereign of the Seas"**	76.80	11.40	0.18	0.39	27.6
38	Oil Tanker–Mont**	458.45	8.33	0.15	0.07	32.3
39	Francisco High-Speed Ferry**	99.0	26.65	0.03	0.75	132.2
40	Hydrofoil craft PTS 150 MK III**	43.22	18.78	0.33	1.00	16.2
41	"Harmony of the Sears"**	362.12	11.83	0.13	0.12	36.7
42	Rowing LM1x Lightweight Men Single**	7.90	4.96	0.03	0.99	126.0
43	Rowing LM4x Lightweight Men 4**	11.78	5.84	0.04	0.86	110.1
44	Male swimming 800 m freestyle*	1.88	1.77	0.20	1.08	25.0
45	Male swimming 50 m freestyle*	1.95	2.38	0.20	1.42	25.1
46	Black marline (*D*/*L* with rostrum)	4.65	29.20	0.16	8.84	30.6
47	Sea glider**	1.80	0.25	0.17	0.16	29.0

І.Г. Нестерук

МАКСИМАЛЬНА ШВИДКІСТЬ ПІДВОДНОГО РУХУ

Проблематика. Зростаючий інтерес до безпілотних підводних транспортних засобів зумовлює посилення уваги до плавання водних тварин. Їхня висока швидкість продовжує дивувати дослідників. Зокрема, велика швидкість дельфіна викликала низку спроб пояснити цей парадокс, що тривають і донині. Деякі дослідники вважають, що навіть тверді тіла, схожі на водних тварин, забезпечують безвідривний режим обтікання, на відміну від поширеного погляду про неминучий відрив. Можливим поясненням може бути ідеальна форма тіла, яка забезпечує обтікання без відриву примежового шару. Видовжені безвідривні форми можуть не тільки зменшити опір тиску, але й затримати ламінарно-турбулентний перехід у примежовому шарі, значно зменшивши опір тертя. Таким чином, очікується, що найбільшу можливу швидкість плавання мають водні тварини.
Мета. Ми спробуємо довести, що низький опір та велика швидкість водних тварин забезпечуються лише їхньою безвідривною формою (що вважається жорстким тілом), тоді як гнучкість і податливість є несуттєвими факторами.
Методика реалізації. Ми будемо використовувати: а) обчислення форми спеціальних тіл обертання з від'ємним градієнтом тиску біля хвоста, схожих на тулуби риб, із застосуванням раніше розроблених методик; б) відомі оцінки опору таких форм для ламінарних і турбулентних випадків; в) енергетичний баланс плавання і теорію ідеального гвинта; г) статистичний аналіз наявних даних про довжину, швидкість і видовження водних тварин.
Результати. Швидкість плавання більшості водних тварин пропорційна довжині тіла у степені 7/9. Виняток становить рух китів, що відбувається в турбулентному режимі за надкритичних чисел Рейнольдса.
Висновки. Ідеальні форми тіла більшості водних тварин забезпечують безвідривне ламінарне обтікання. Оцінки максимальної швидкості руху для ламінарного і турбулентного випадків показують, що безвідривні корпуси спеціальної форми можуть значно збільшити швидкість підводних транспортних засобів і SWATH-суден. Подальше збільшення швидкості може бути досягнуте за рахунок використання суперкавітації за більшої, ніж у тварин, потужності-ефективності.

Ключові слова: плавання водних тварин; зменшення опору; безвідривні форми; кавітація; високошвидкісні підводні апарати.

И.Г. Нестерук

МАКСИМАЛЬНАЯ СКОРОСТЬ ПОДВОДНОГО ДВИЖЕНИЯ

Проблематика. Растущий интерес к беспилотным подводным аппаратам обуславливает усиление внимания к плаванию водных животных. Их высокая скорость продолжает удивлять исследователей. В частности, большая скорость дельфина вызвала ряд попыток объяснить этот парадокс, которые продолжаются и по сей день. Некоторые исследователи считают, что даже твердые тела, похожие на водных животных, обеспечивают безотрывный режим обтекания, в отличие от распространенного взгляда о неизбежном отрыве. Возможным объяснением может быть идеальная форма тела, которая обеспечивает обтекание без отрыва пограничного слоя. Удлиненные безотрывные формы могут не только уменьшить сопротивление давления, но и задержать ламинарно-турбулентный переход в пограничном слое, значительно снижая сопротивление трения. Таким образом, ожидается, что наибольшую возможную скорость плавания имеют водные животные.

Цель. Мы попробуем доказать, что низкое сопротивление и большая скорость водных животных обеспечиваются только их безотрывной формой (что считается жестким телом), тогда как гибкость и податливость являются незначительными факторами.

Методика реализации. Мы будем использовать: а) вычисления формы специальных тел вращения с отрицательным градиентом давления у хвоста, похожих на туловища рыб, с применением ранее разработанных методик; б) известные оценки сопротивления таких форм для ламинарных и турбулентных случаев; в) энергетический баланс плавания и теорию идеального винта; г) статистический анализ имеющихся данных о длине, скорости и удлинении водных животных.

Результаты. Скорость плавания большинства водных животных пропорциональна длине тела в степени 7/9. Исключение составляет движение китов, которое происходит в турбулентном режиме при сверхкритических числах Рейнольдса.

Выводы. Идеальные формы тела большинства водных животных обеспечивают безотрывное ламинарное обтекание. Оценки максимальной скорости движения для ламинарного и турбулентного случаев показывают, что безотрывные корпуса специальной формы могут значительно увеличить скорость подводных транспортных средств и SWATH-судов. Дальнейшее увеличение скорости может быть достигнуто за счет использования суперкавитации при большей, чем у животных, мощности-эффективности.

Ключевые слова: плавание водных животных; снижение сопротивления; безотрывные формы; кавитация; высокоскоростные подводные аппараты.